NBSIR 79-1904 (Navy)

Passive Films, Surface Structure and Stress Corrosion and Crevice Corrosion Susceptibility

J. Kruger, J. J. Carroll, A. J. Melmed
J. J. Ritter, and J. R. Ambrose

Chemical Stability and Corrosion Division
and
Surface Science Division
National Bureau of Standards
U.S. Department of Commerce
Washington, D.C. 20234

November 1979

Technical Summary Report No. 9

Prepared for
Office of Naval Research
Department of the Navy
Arlington, VA 22217

NBSIR 79-1904 (Navy)

PASSIVE FILMS, SURFACE STRUCTURE AND STRESS CORROSION AND CREVICE CORROSION SUSCEPTIBILITY

J. Kruger, J. J. Carroll, A. J. Melmed
J. J. Ritter, and J. R. Ambrose

Chemical Stability and Corrosion Division
and
Surface Science Division
National Bureau of Standards
Washington, D.C. 20234

November 1979

Prepared for
Office of Naval Research
Department of the Navy
Arlington, VA 22217

U.S. DEPARTMENT OF COMMERCE

Luther H. Hodges, Jr., *Under Secretary*

Jordan J. Baruch, *Assistant Secretary for Science and Technology*

NATIONAL BUREAU OF STANDARDS, Ernest Ambler, *Director*

PART I - The Study of the Early Stages of Hydrogen Embrittlement of Some Metals and Alloys Using Field Ion Microscopy

J. J. Carroll, A. J. Melmed
Surface Science Division

and

J. Kruger
Chemical Stability and Corrosion Division
National Bureau of Standards
Washington, D.C. 20234

INTRODUCTION

Field ion microscopy (FIM) is capable of imaging defects such as sub-critical crack formation and growth, and surface rearrangements, and of detecting new surface phase formations, and other disturbances. Thus, we have used the technique to characterize various modes of hydrogen reactions with metal surfaces. (1-3) Previous work from this laboratory has revealed examples of one mode, the initial crack formation and growth in the hydrogen-titanium(1) and hydrogen-zirconium(2) systems. In each case there were indications of preferential crystallographic attack producing cracks within the metal matrix approximately 10-15 atomic layers deep in the case of titanium, and 2-5 layers deep in the case of zirconium. We also have shown in the hydrogen-uranium system,(3) under similar conditions of temperature and pressure, that another mode of hydrogen attack occurred — surface film formation of a reaction product. An orthorhombic single crystal of uranium (micrographs obtained using inert imaging gases) exposed to hydrogen, initially formed a disordered film, and, after prolonged hydrogen interaction, formed nuclei that eventually coalesced into a small grained (5-30 nm, lateral dimensions) film of what may likely be uranium hydride. Field evaporation of the overlayer phase revealed a crack-free uranium substrate. An example of qualitatively less metal attack due to hydrogen was found in the hydrogen-iron system where FIM studies(3) showed nonuniform surface damage that did not extend deeply into the iron substrate. The (111) plane areas were the most sensitive and appeared highly disordered and were probably structurally rearranged, whereas the (100) plane areas remained ordered, and the (110) plane areas showed intermediate damage. FIM studies of 1080 carbon steel(3) did not reveal any adverse effects due to hydrogen, even with specimens having grain boundaries intersecting the surface.

In the present phase of the work, FIM was used to examine microscopic details of the initial stages of hydrogen interactions with some additional pure metals and metal alloys, i.e., niobium, aluminum, 304 stainless steel and iron-24 wt. % chromium steel. The hydrogen-metal interactions occurred during the FIM imaging process with hydrogen pressures between 10^{-4} and 10^{-6} torr at metal temperatures between 20 and 80 K, and while the metal was subjected to stresses brought about

by the electric field necessary for imaging the multifaceted, approximately hemispherical metal surface. The method used involved comparison of micrographs obtained during inert gas imaging (neon, helium) with micrographs obtained in pure hydrogen or mixtures of hydrogen and inert gases. Usually FIM provides information regarding intragranular crack formation except for the relatively rare circumstance of a grain boundary intersecting the metal surface in the field of view. The objective of the present work is to explore the different modes of hydrogen interactions with metals and alloys using FIM in order to better understand the mechanisms that lead to metal fracture. Materials chosen for this study are listed in Table 1. Niobium was chosen as an example of a metal that is known to form an embrittling hydride.(4) The aluminum and 304 stainless steel studies were made to throw some light on the controversy(5,6) regarding the question of whether these face-center-cubic metals suffer hydrogen damage — an important factor in determining the mechanisms of stress corrosion cracking. Finally, experiments were performed with iron-24% chromium specimens to determine the structural effects incurred by pretreating the specimens with various cathodic charging doses of hydrogen. The results demonstrate that FIM is a powerful method for studying the important metallurgical problem of hydrogen embrittlement.

EQUIPMENT

The field ion microscope was equipped with a 90 mm diameter microchannel plate image intensifier, and a specimen-quick-change chamber for rapid specimen insertion and withdrawal. Routinely, images from two specimens could be obtained within a half an hour's time. This was an important advantage in the studies involving hydrogen interaction with several types of specimens, such as pure metals and alloys subjected to a variety of environmental and preimaging treatments to promote hydrogen-metal interactions. Furthermore, the images obtained were generally unstable, thus requiring image intensification in order to achieve fractional second, photographic exposure times. The specimen temperatures were controlled by adjusting the flow of cold gaseous helium from a liquid helium dewar flask over the specimen-mount-feed-through pin. During field ion microscopy reagent grade imaging gases were continuously flowed through the imaging chamber. Imaging gas mixtures were made by simultaneously opening the appropriate leak valves, and mixture compositions were estimated from pressure gauge measurements.

SPECIMENS

TABLE I

Starting Material and Specimen Preparation Procedures
for Imaging in the Field Ion Microscope

	Material	Tip Sharpening Procedure
1.	niobium 5 mil diam. wire	a) plastic dish containing conc. H_2SO_4 at about 1-1/2" depth followed with about 10 drops of 48% HF, leave unmixed, about 7.5 Vdc; b) wash in water followed by methanol.
2.	aluminum 5 mil diam. wire	a) reduce diam. and taper, 10% $HClO_4$ in methanol, 15 - 10 Vac; b) polish to a sharp point, thin liquid film of 1% $HClO_4$ in glycerin, 30 Vac, while observing at 100 X; c) frequent methanol washes during and after parts a) and b).
3.	304 stainless steel 5 mil diam. wire	a) reduce diam. and polish to a sharp point in 10% $HClO_4$ in methanol, 50 Vdc OR sharpen tip in 10% HCL, aqueous thin liquid film while observing at 100 X; b) frequent methanol washes during and after parts a) and b).
4.	iron - 24 wt. % chromium 20 mil diam. rods spark cut from ingot	a) reduce diam. and taper, 10% $HClO_4$ in methanol, 12-2 Vdc; b) polish to a sharp point, thin liquid film of 1% $HClO_4$ in glycerin, 2 Vdc while observing at 100 X; c) frequent methanol washes during and after parts a) and b).

NIOBIUM

Niobium images obtained with neon and neon-helium mixtures (Figs. 1a, 1d) were stable and showed long range bcc crystal order. The field ion micrograph of Fig. 1a was obtained from a niobium sample not previously exposed to hydrogen imaging conditions in the microscope. The micrograph shows many lattice defects including several spiral dislocations. Most likely, these were inherent crystal defects in the sample. Potentially, the defects provided easy access routes for hydrogen and rendered the sample more susceptible to attack in subsequent experiments with hydrogen.

Fig. 1b is a hydrogen field ion micrograph obtained from the same specimen as in Fig. 1a. As opposed to images obtained with inert gases, the hydrogen images were unstable, with most spots often appearing and disappearing and with overall image appearance of liquid-like movement. The formerly long range crystal order was reduced to relatively short range order. The micrograph of Fig. 1b shows many groupings of spots ranging from 2 to 15-20 spots per group. The groups appear delineated by relatively dark, non-spotty lines appearing wider than those between resolved spots within a group. Some groups show ordered spot arrangements. For example, there are areas where spots form arcs that seem to partially mimic concentric rings. The evidence suggests that hydrogen was interacting with the niobium surface and formed a surface compound.

Subsequently, the hydrogen imaging gas was removed, and the neon field ion micrograph of Fig. 1c was obtained after partially evaporating the surface layer formed during the previous hydrogen-niobium interaction. Some underlying substrate crystal planes are in evidence at the upper and lower left portions of the micrograph along with the relatively disordered surface layer. The micrograph indicates that the residual adsorbed film was partially stripped away with no sign of more permanent bulk defects in niobium brought about by the hydrogen interaction. Typically, as the electric field was necessarily increased to image with neon after a hydrogen treatment, the adsorbed layer was observed to evaporate quickly.

The neon field ion micrograph of Fig. 1d was obtained after the surface layer was completely removed by field evaporation. The micrograph does not show any residual damaging effects to the niobium substrate. The spiral dislocations remain in place.

Therefore, these experiments indicate that niobium, although suffering surface damage from hydrogen, does not seem to undergo crystallographically selective, deep damage as found in titanium(1) and zirconium(2) under similarly low temperatures and hydrogen pressures. This statement is tentative pending further examination of other niobium specimens. Future studies will proceed in an effort to initiate hydrogen embrittlement by systematically increasing the severity of the hydrogen-niobium interaction. For example, niobium specimens precharged with as much as 2 atomic % hydrogen are known to fracture at 277 K.(4)

ALUMINUM

Aluminum is an example of a material that exhibits extreme instability at neon imaging field conditions in the unbaked field ion microscope with specimens cooled with liquid nitrogen. Aluminum under these conditions is far more unstable than 1080 steel imaged with hydrogen at room temperature.(3) The neon images obtained from aluminum near liquid nitrogen temperature are not typical of field ion images showing resolved surface atoms but, instead, are similar to aluminum field desorption images,(7-9) usually obtained with a double channel plate and without imaging gas. The image shown in Fig. 2 was obtained from an aluminum specimen neon field evaporating hundreds of layers during the 1/10 s film exposure time. The crystal directions and zone lines appear relatively dark against an overall gray background. Disparties between published desorption images(7-9) and those in Fig. 2 occur about the <100> direction where four relatively bright (instead of dark) lines are symmetrically disposed. This as well as the few bright spots distributed about the surface do not appear in the normally derived field desorption patterns(7-9) and are ascribed to artifacts associated with the neon imaging gas.

By cooling from about 80 to 30 K, aluminum was nearly stabilized (slowly field evaporated) under imaging conditions and became accessible to neon field ion microscopy. Fig. 3 compares favorably with previously published neon field ion micrographs of aluminum(10,11) in that it shows overall crystal order. The (111) and (100) plane areas are not normally imaged fully in neon.(10,11) However, in the (110) and higher index plane areas (Fig. 3), there appears to be relatively short, dark lines that interrupt the ordered concentric rings of atoms. These minor line defects brought about by atomic vacancies are not found in the published micrographs(10,11) that were obtained using a baked field ion microscope. The evidence suggests that these defects and aluminum's slight instability during neon imaging may be due to residual hydrogen in the background vacuum at low partial pressures.

Hydrogen field ion images of aluminum (Fig. 4a) are composed of small areas marked by boundaries, sometimes showing ordered square arrays of spots and partial concentric rings, indicating that hydrogen may have chemically interacted with aluminum surface atoms to form another surface phase. Fig. 4b is a neon field ion micrograph of the previously formed hydrogen-aluminum interactive layer obtained after removing the hydrogen imaging gas and partially evaporating some of the interacted layer at the higher neon imaging fields. The long line defects are present in the micrographs of Figs. 4a and 4b but have disappeared in the image of Figure 4d. The micrographs in Fig. 4 occurred sequentially and were selected from a larger group. They are collectively interpreted as indicating that the observed line defects originate in the aluminum-hydrogen interacted layer and do not extend very deeply into the aluminum substrate. Furthermore, Fig. 4c shows atomic resolution in the normally darkened (100) and (111) plane areas. This indicates that hydrogen adsorbed on aluminum aids in neon imaging of the (100) and (111) plane areas.

Interesting surface effects were observed by imaging aluminum specimens with mixtures of hydrogen and neon (Fig. 5). Hydrogen promotes imaging of the aluminum (100) and (111) plane areas but also promotes formation and field evaporation of the aluminum-hydrogen interacted layer. The micrographs in Fig. 5 were obtained during field evaporation. As opposed to imaging with pure hydrogen (Fig. 4a), lower partial pressures of hydrogen in the imaging gas mixtures prevent thicker film formations to occur that obscure the symmetry of the aluminum substrate. Nevertheless, the micrographs (Fig. 5) demonstrate that there is a multitude of surface defect effects brought about by the presence of hydrogen.

Aluminum field ion micrographs obtained with hydrogen-helium mixtures (Fig. 6) show more crystalline order than micrographs obtained with hydrogen-neon mixtures (Fig. 5) indicating that the hydrogen-aluminum interacted layer is less extensive. There are more higher index planes visible with concentric rings and fewer surface defects. Usually, there are only a few concentric rings about a crystal direction before the atom spots become more randomly arranged. It is in these areas where surface defects appear and are typical of those found in hydrogen-neon field ion micrographs of aluminum. Occasionally, long line defects occur that cut across crystal planes. Future attempts to image aluminum alloys may be realized best by using hydrogen promoted field ion microscopy, that is using small traces of hydrogen in an otherwise inert image gas.

It is clear from these studies with aluminum that significant but not deep surface defects occur in the presence of hydrogen and the tensile stress brought about by the imaging electric field. Quantitative determinations of depths to which the defects penetrate the aluminum lattice have yet to be made. (Qualitatively, they appear to be less deep than those found in the hydrogen-titanium(1) system.) This is a more difficult matter that may require the use of a baked field ion microscope, in the light of aluminum's sensitivity to hydrogen. Of course, field-ion-atom-probe-mass-spectrometry(12) would provide very useful information regarding the chemical identity of the imaged species in the immediate vicinity of the observed defects.

304 STAINLESS STEEL

Like aluminum, this alloy was suggested as one in which the mechanism of stress corrosion cracking involves hydrogen embrittlement.(6) It was previously shown(3) that field ion micrographs of 304 stainless steel exhibited, generally, more disordered imaged areas than found in 1080 high strength carbon steel and iron-24% chromium steel. The better micrographs(13) showed evidence of grain boundaries and some short-range order (crystal net plane rings immersed in an array of disordered spots). When that particular grain was reduced in size by further field evaporation (Fig. 7a), the smaller grain (brighter spots) showed long-range order, but the larger grain (Figs. 7a and b) showed only short-range

order. The particle imaged in Fig. 7a was probably an unmixed alloy constituent of dimensions approximately 22 x 38 nm. Micrographs intermediate between Figs. 7a and b show it as small as 5 nm in diameter.

It is possible that artifacts may give rise to relatively disordered field ion images of materials that would otherwise appear ordered. These include (a) premature field evaporation of some alloy constituents leaving vacancies, (b) significantly different best imaging fields among the various alloy constituents thereby causing only some to be imaged, and (c) especially persistent adsorbed films covering the sought-after substrate.

On the assumption that the latter condition prevailed in the case of 304 stainless steel, the technique of manually pulsed field ion imaging was attempted and exhaustively explored without successfully improving image quality. The technique is known to be successful in removing persistently adsorbed films from iron-24% chromium and uranium at 30 K.(3) During the high electric field pulse, specimens are dramatically destabilized and several hundred layers are quickly field evaporated. Following the pulse, the applied voltage is restored to one for best imaging. The specimen is stabilized and, momentarily, is in a relatively film-free state. Unfortunately, no firm conclusions may be drawn from the above results.

However, more rewarding results were obtained from 304 stainless steel wires that were vacuum annealed (about 800 to 1000C for four hours and quickly cooled) before field ion emitters were prepared from them. Annealing temperatures were high enough so as not to promote sensitization (precipitation at grain boundaries) and long enough to promote grain growth without crystal structure changes. The hydrogen ion images in Fig. 8 demonstrate the improved image quality that results from preannealing the wires. Apparently, in degassed specimens (annealed), a more unobstructed image of the alloy surface is obtained; whereas, in unannealed specimens, some imaging of dissolved gases occurs and introduces apparent disorder. There are a great many boundaries in evidence in Fig. 8b and in a subsequently obtained helium-neon ion micrograph of the same specimen. (Note the regions indicated in Fig. 8c). Their origin remains unclear, but, nevertheless, the boundaries could indicate the initial formation of martensite, which a number of workers suggest is involved in the stress corrosion of 304 stainless steel by a hydrogen embrittling mechanism. In addition to determining crystal structure of the regions contained within the boundaries, it would be useful in future studies to examine 310 stainless steel because, as opposed to 304, it is known(14) not to form martensite in the presence of hydrogen and stress.

IRON-24 wt. % CHROMIUM

This final segment reveals the kinds of effects brought about by a series of cathodic hydrogen charging experiments on previously field

evaporated and characterized iron-24 wt. % chromium surfaces. The necessary control experiments with alloy specimens not subjected to cathodic polarization showed minimal effects.

Fig. 9 shows examples of neon field ion micrographs obtained from liquid nitrogen cooled iron-24 wt. % chromium. Images were slightly unstable and slowly field evaporated at best image voltages. Overall, specimens exhibited cubic symmetry with four (111) plane areas about a central (100) plane. Some specimens were vacuum annealed prior to tip manufacture, and the microscope vacuum system was subjected to varying degrees of gettering without effecting change in the following two features of the micrographs. (1) The presence of dark, non-imaging areas predominantly appearing in the central region of the micrographs — corresponding to the tip apex and indicating preferential attack and field evaporation in the [110]-[100] zone lines and (110) planes. The recessed surface atoms may then be field shielded by the outer shell of imaging atoms and, thereby, not exposed to the high electric fields necessary for neon imaging. (2) The presence of numerous line defect boundaries distributed about the imaged surface, not unlike those found on aluminum specimens imaged in neon-hydrogen mixtures (Fig. 5) and, to a lesser extent in the neon ion micrographs of aluminum (Fig. 3). The cause of these defects may be low partial pressures of active gases, such as hydrogen, water vapor and oxygen, in the microscope's base vacuum.

Liquid nitrogen cooled iron-24 wt. % chromium specimens imaged with hydrogen (Fig. 10a) were stable and did not field evaporate at imaging voltages. Overall, the (111) planes appear to chemically interact the least with hydrogen imaging gas, as evidenced by the preservation of their concentric ring appearance. The centrally located [110]-[100] zone lines and (110) planes show non-ordered imaging spots. This specimen previously imaged with neon showed no imaging points in these same areas. Possibly, under hydrogen imaging conditions, the supposedly recessed [110]-[100] zone lines and (110) planes became visible via a hydrogen adsorbed layer. In cases where iron-24% chromium was reimaged with neon following hydrogen ion microscopy (Fig. 10b), it was necessary to remove several tens of layers of (111) planes before zone line darkening would begin to reappear (Fig. 10c). Although it might seem that the prior hydrogen interactions caused extensive damage in these areas, we prefer, instead, to interpret persistent zone line and (110) plane imaging after a hydrogen exposure as arising from residual hydrogen promoting neon imaging of these areas. Similar zone line imaging occurred with controlled mixtures of hydrogen and neon.

In another approach to the hydrogen-iron-24% chromium interaction, additional experiments were carried out that explored the effects of cathodically charging the alloy lattice with hydrogen. Typically, liquid nitrogen cooled specimens were initially characterized (field evaporatored) in neon and/or hydrogen. The field evaporated tip was

removed from the microscope, dipped and withdrawn from a 10% aqueous perchloric acid solution under an applied voltage at room temperature, and subsequently reimaged near 80 K in the field ion microscope. A platinum counter-electrode was used, and the applied voltage and immersion time were varied. Following cathodic polarization, micrographs were obtained with hydrogen since all specimens catastrophically fractured near neon imaging fields. As summarized in Table II, the results obtained varied from little to no detectable alloy surface damage at 10 Vdc, 4s, to film formation without significant substrate damage at 10 Vdc, 4 min., and significant substrate damage without film formation at 20 Vdc, 4 min.

TABLE II

Annotations from FIM Studies of Cathodically Charged Iron-24 wt. % Chromium Specimens in Aqueous Solutions of 10% Perchloric Acid Solution Versus a Platinum Counter-Electrode.

Series	Applied Volts (dc)	Exposure Time	Remarks
a	10	4 s	no significant surface damage (Fig. 11)
b	10	1 min	no significant surface damage
c	10	2 min	considerable tip blunting with surface damage (Fig. 12)
d	10	4 min	film formation without detectable substrate damage
e	10	8 min	film formation without significant substrate damage (Fig. 13)
f	20	4 min	great alloy surface damage without film formation (Fig. 14)

Figs. 11a and b show hydrogen and neon ion micrographs of an iron-24% chromium specimen obtained prior to cathodic polarization in series a. Figs. 11c through f are hydrogen ion micrographs obtained at progressively higher voltages directly after cathodic polarization. The images of Figs. 11c and d were unstable and typical of those showing fleeting image points from a desorbing accumulation. The image of Fig. 11e showed the first signs of surface order and increased stability of imaging points. The left crescent shaped area of spots came from an area of residual accumulation that was not field evaporated. Some spots in this area appear as large doublets and quadruplets and are similar in appearance to those in Figs. 11c and d. Note that the transient image spots and the crescent shaped area in Fig 11e are not present in Fig. 11 F. These accumulations are usually short lived in the field ion microscope and are distinguished from more permanent film formations (probably thicker) that occurred in series d and e. A fully field evaporated hydrogen ion image of the alloy surface in Fig. 11f shows evidence of a disturbed (111) plane cut by a possible grain boundary.

The sequence of hydrogen ion micrographs in Fig. 12 was obtained from series c with micrograph 12a obtained before cathodic polarization. Figs. 12c and d show evidence of surface damage in the dark lined areas. However, the origin of these defects is inconclusive since a tear-off

event occurred between Figs. 12b and c. A tear-off event is defined as an uncontrolled field evaporation of a material during imaging. This was the only series of the 10 V set in which a tear-off event occurred as well as detectable alloy surface damage and a relatively large increase in average specimen radius after cathodic polarization.

The sequence of hydrogen ion micrographs in Fig. 13 was obtained from series e. An interesting feature in this set is the presence of a boundary, bisecting the image in Fig. 13a — obtained before cathodic polarization, showing apparently dissimilar coverages in Figs. 13b and c — consecutively obtained after cathodic polarization, and persisting after film removal. The sequence of micrographs was obtained at progressively higher voltages. Fig. 13d shows a stage in which the adsorbed film (Figs. 13b and c) receded from the central area of the micrograph to reveal the underlying substrate.

Fig. 14 shows a sequence of hydrogen ion micrographs obtained from series f. In this case there was no evidence of an adsorbed film since the images obtained after cathodic polarization immediately showed ordered substrate areas. The micrographs clearly show great surface damage, far in excess to that observed in series a through e. Several tens and possibly hundreds of layers were evaporated without successfully removing some of the more deeply damaged areas.

In summary, it was demonstrated that FIM detected a spectrum of surface effects brought about by a broad brush variation of cathodic polarization conditions in iron-24% chromium. It is desirable, however, to remove hydrogen from all post-cathodic polarization imaging because a) hydrogen is the agent promoting hydrogen embrittlement, and b) neon ion micrographs show more clearly the line defects inherent in the material. Since all cathodically polarized specimens failed at the higher stresses associated with the larger imaging fields necessary for neon imaging, it suggests that smaller hydrogen charging doses are necessary to avoid failure at neon imaging fields. To this end, future FIM experiments will be directed.

From the preceding work it is clear that FIM is capable of characterizing different modes of hydrogen interactions with metals under stress. Although present studies were limited to a relatively low temperature regime, it should be possible in future work to stress-interact at room temperature with intermittent low temperature microscopy at least with materials more refractory than aluminum.

REFERENCES

(1) J. J. Carroll, J. Smit, and A. J. Melmed, "Field Ion Imaging of Titanium and Effects Due to Hydrogen", Surface Sci. 45 (1974) 640-8.

(2) J. J. Carroll and A. J. Melmed, "Field Ion Microscopy of Zirconium", Surface Sci. 58 (1976) 601-4.

(3) J. J. Carroll, A. J. Melmed, and J. Kruger, "Field Ion Microscopy Studies of the Interaction of Hydrogen with Selected Metals and Alloys", in: The Role of Passive Film Growth Kinetics and Properties in Stress Corrosion and Crevice Corrosion Susceptibility, NBSIR 78-1429, Part I, (May 1978) 1-16.

(4) M. L. Grossbeck, P. Williams, C. A. Evans, Jr., and H. K. Birnbaum, "Application of Ion Probe Analysis to Studies of Hydrogen Behavior in Solids", Phys. Stat. Sol. (a) 34 (1976) K97-9.

(5) R. J. Gest and A. R. Troiano, "Stress Corrosion and Hydrogen Embrittlement in an Aluminum Alloy", Corrosion 30 (1974) 274-9.

(6) R. W. Staehle, "Stress Corrosion Cracking of the Fe-Cr-Ni Alloy System", in: The Theory of Stress Corrosion Cracking in Alloys, J. C. Scully, Editor, (N.A.T.O., Brussels, 1971), 221-286.

(7) E. D. Boyes, A. R. Waugh, P. J. Turner, P. F. Mills, and M. J. Southon, in: Developments in Electron Microscopy and Analysis, 1977, (EMAG 77), D. L. Misell, Editor, Inst. Phys. Conf. Ser. No. 36 (1977) Chapter 9, 343-6, (Fig. 4).

(8) A. R. Waugh, E. D. Boyes, and M. J. Southon, "Investigations of Field Evaporation with a Field-desorption Microscope", Surface Sci. 61 (1976) 109-142, (Figs. 3 and 6).

(9) M. J. Southon, E. D. Boyes, P. J. Turner, and A. R. Waugh, "Some Applications of Field-ionization and Field-evaporation Techniques in the Study of Surfaces", Surface Sci. 53 (1975) 554-580, (Fig. 11).

(10) Ref. 9, (Fig. 4)

(11) W. Zingg and H. Warlimont, "On Imaging of Aluminum by Field Ion Microscopy", Phys. Stat. Sol. (a) 45 (1978) 117-122, (Fig. 2).

(12) E. W. Müller and T. T. Tsong, Field Ion Microscopy; Principles and Applications (Elsevier, New York, 1969), pp. 130-4.

(13) Ref. 3, (Fig. 7).

(14) M. L. Holzworth, "Hydrogen Embrittlement of Type 304L Stainless Steel", Corrosion 25 (1969) 107-115.

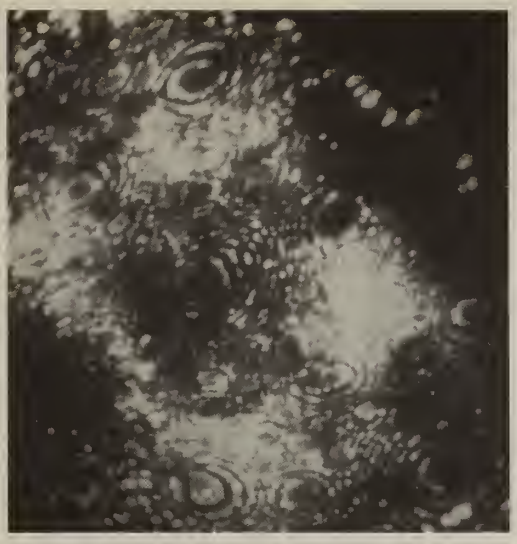

(a)

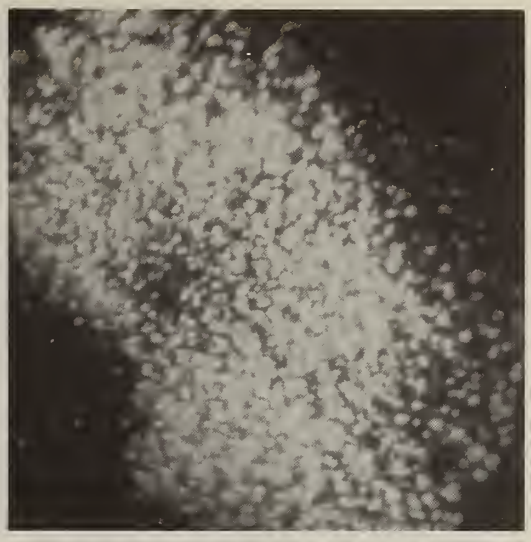

(b)

(c)

(d)

Fig. 1. Consecutive field ion micrographs obtained from the same niobium specimen, liquid nitrogen cooled. (a) neon image, 14,500 volts; (b) hydrogen image, 8,800 volts; (c) neon image, 13,300 volts; and (d) neon image, 14,200 volts.

Fig. 2. Neon image obtained from liquid nitrogen cooled aluminum, about 13,000 volts.

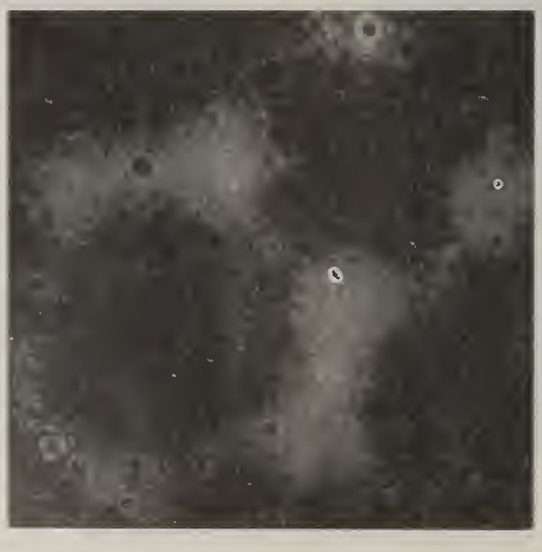

Fig. 3. Neon field ion micrograph obtained from aluminum, 30 K, 12,000 volts.

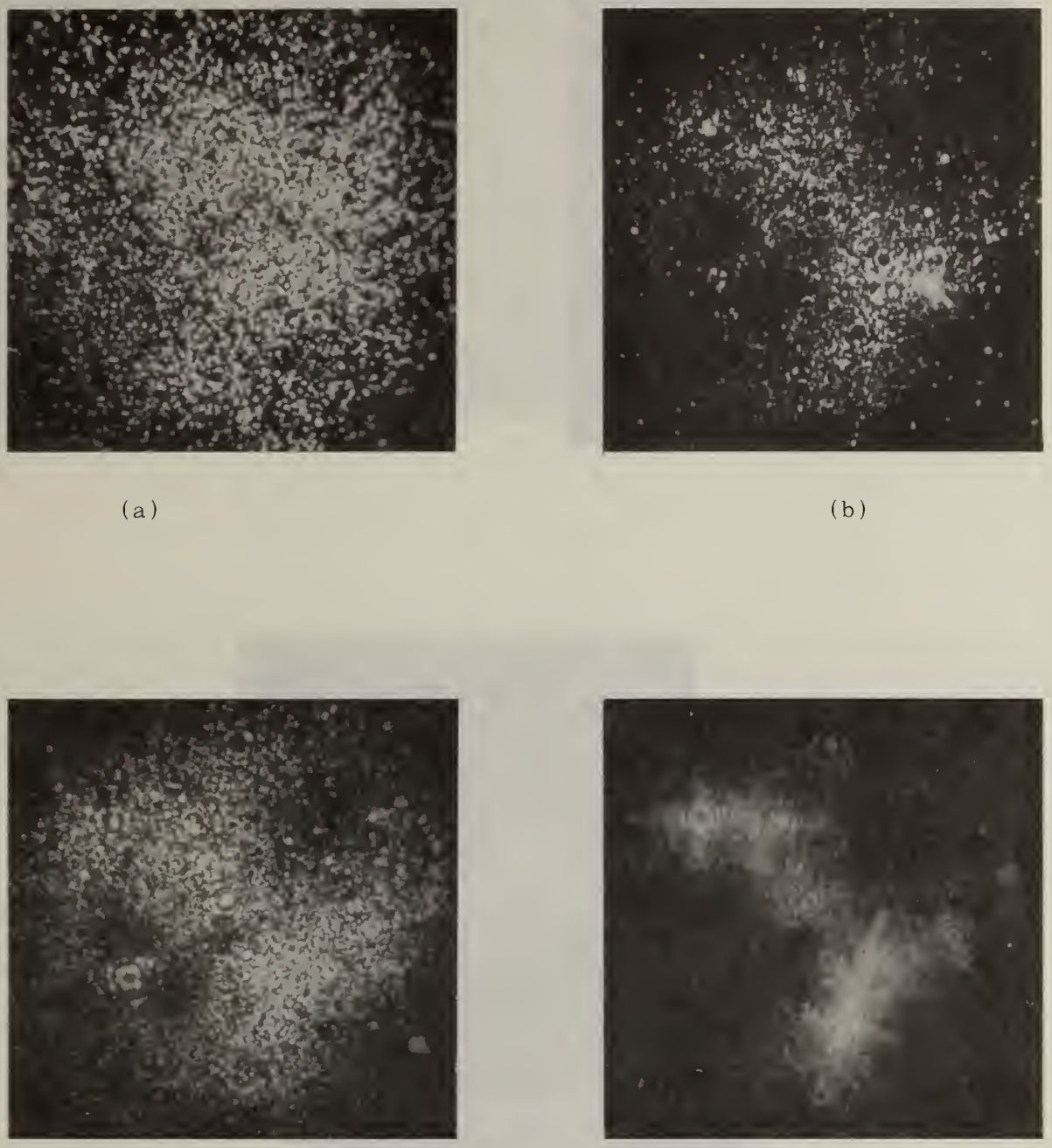

(a) (b)

(c) (d)

Fig. 4. Consecutive field ion micrographs obtained from the same specimen of aluminum, 30 K. (a) hydrogen image, 7000 volts; (b) and (c) neon image, 10,700 volts; (d) neon image, 12,000 volts.

(a)

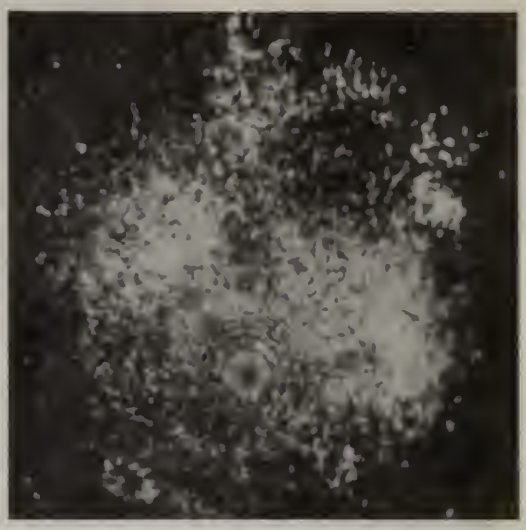

(b)

(c)

Fig. 5. Aluminum field ion micrographs obtained with neon-hydrogen gas mixtures, 30 K. (a) 4600 volts; (b) 4700 volts; (c) 7850 volts.

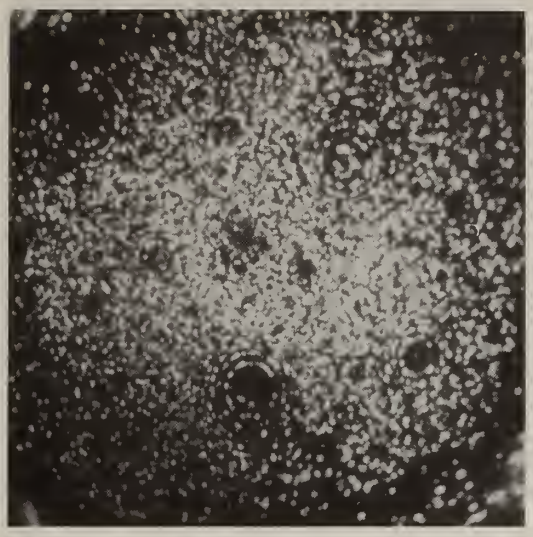

(a)

(b)

Fig. 6. Aluminum field ion micrographs obtained with helium-hydrogen gas mixtures, 30 K. (a) 7300 volts; (b) 13,000 volts.

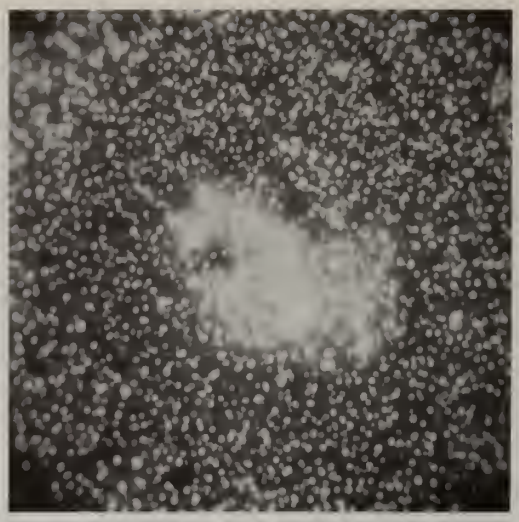

(a)

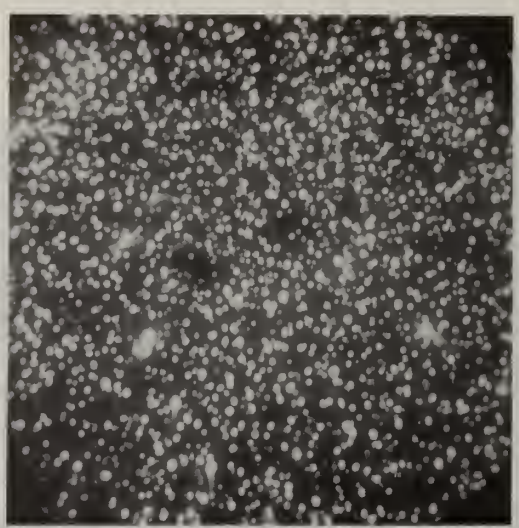

(b)

Fig. 7. Consecutive field ion micrographs [(a), (b)] obtained from an unannealed 304 stainless steel specimen imaged with a neon-helium gas mixture, 30 K, 12,500 volts.

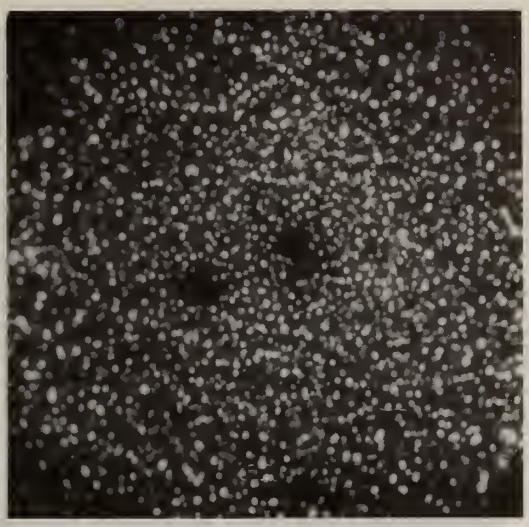

(a)

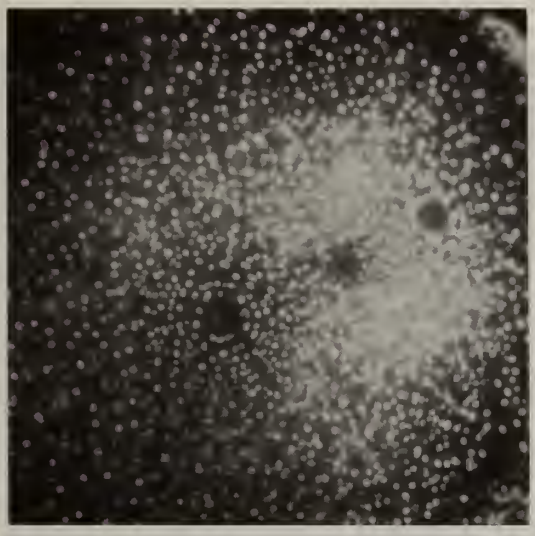

(b)

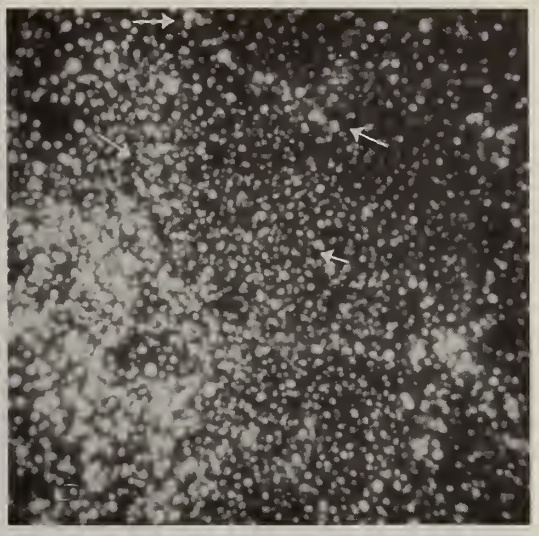

(c)

Fig. 8. 304 stainless steel field ion micrographs (a) unannealed specimen imaged with hydrogen, 30 K, 6900 volts; (b) annealed specimen imaged with hydrogen, 30 K, 4700 volts; (c) annealed specimen imaged with a neon-helium gas mixture, 30 K, 7800 volts.

(a)

(b)

Fig. 9. Neon field ion micrographs obtained from iron-24% chromium, liquid nitrogen cooled. (a) 8800 volts; (b) 14,500 volts.

(a)

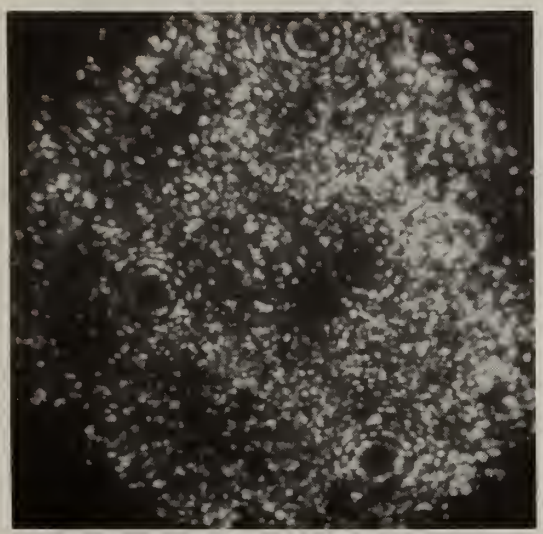

(b)

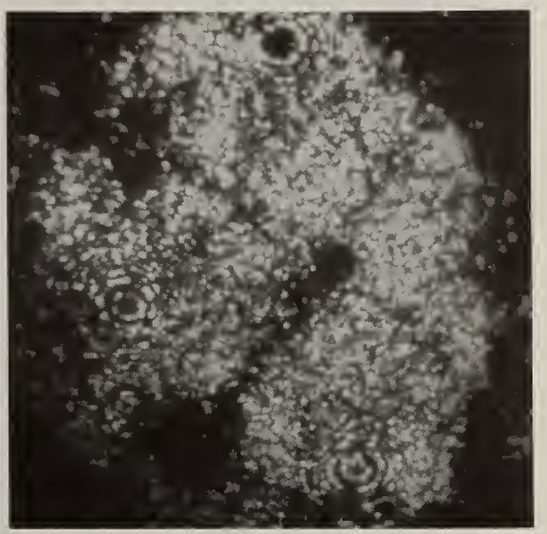

(c)

Fig. 10. Consecutive field ion micrographs obtained from the same specimen of iron-24% chromium, liquid nitrogen cooled. (a) hydrogen image, 10,300 volts; (b) neon image, 14,800 volts; (c) neon image, 15,200 volts.

(a)

(b)

(c)

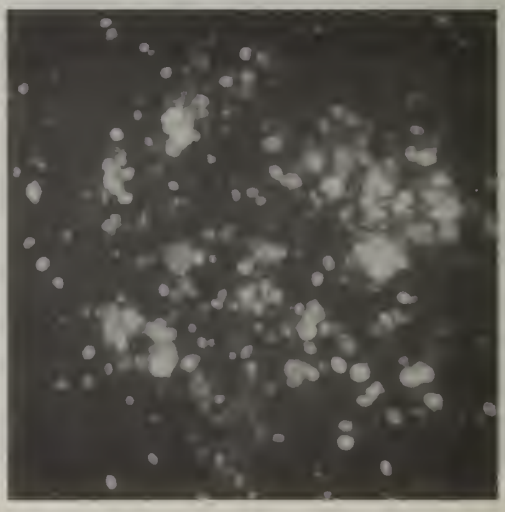

(d)

Fig. 11.

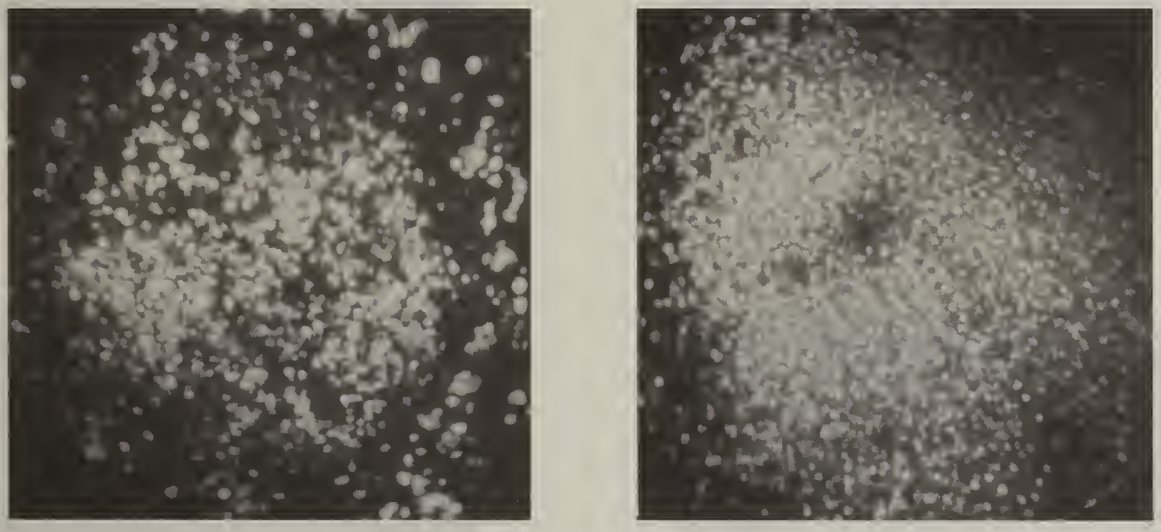

(e) (f)

Fig. 11. Consecutive field ion micrographs obtained from the same iron-24% chromium specimen, liquid nitrogen cooled. (a) hydrogen image, 8000 volts; (b) neon image, 12,400 volts. Hydrogen field ion micrographs (c) through (f) obtained after cathodic polarization, series a, Table II. (c) 4900 volts; (d) 5900 volts; (e) 6800 volts; (f) 8100 volts.

(a)

(b)

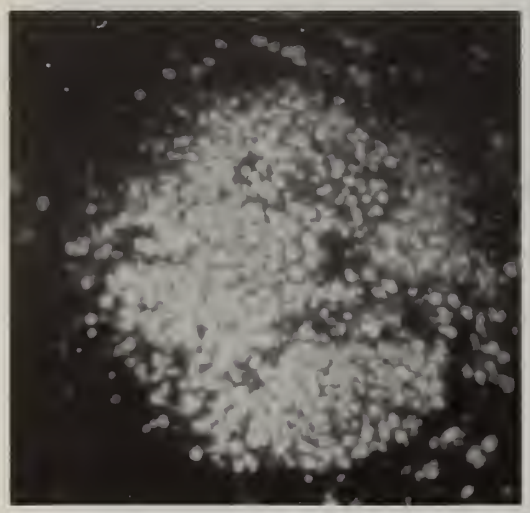

(c)

(d)

Fig. 12. Consecutive field ion micrographs obtained from the same iron-24% chromium specimen, liquid nitrogen cooled. (a) hydrogen image, 6500 volts. Hydrogen field ion micrographs (b) through (d) obtained after cathodic polarization, series c, Table II. (b) 7000 volts; (c) and (d) 7700 volts.

(a)

(b)

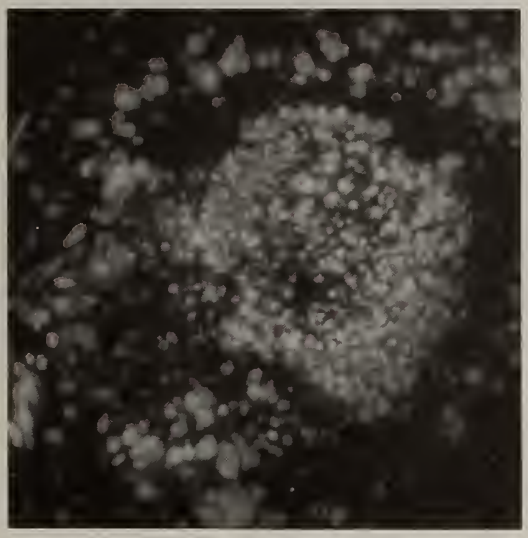

(c)

(d)

Fig. 13. Consecutive field ion micrographs obtained from the same iron-24% chromium specimen, liquid nitrogen cooled. (a) hydrogen image, 7800 volts. Hydrogen field ion micrographs (b) through (d) obtained after cathodic polarization, series e, Table II. (b) 6700 volts; (c) 7100 volts; (d) 8000 volts.

(a)

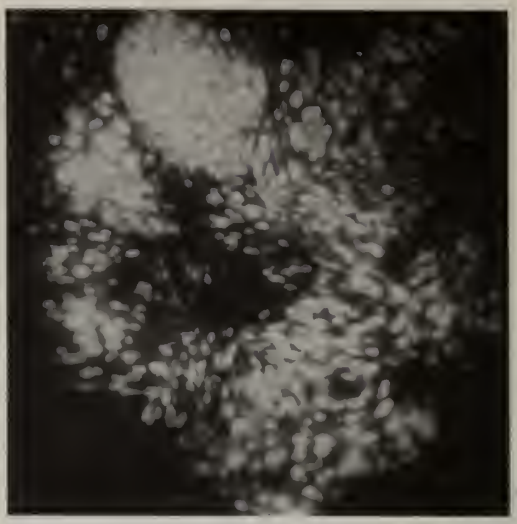

(b)

(c)

(d)

Fig. 14. Consecutive field ion micrographs obtained from the same iron-24% chromium specimen, liquid nitrogen cooled. (a) hydrogen image, 8800 volts. Hydrogen field ion micrographs (b) through (d) obtained after cathodic polarization, series f, Table II. (b) 7600 volts; (c) 11,500 volts; (d) 12,900 volts.

PART II

An Improved Triboellipsometric Apparatus

J. J. Ritter and J. R. Ambrose
Chemical Stability and Corrosion Division
National Bureau of Standards
Washington D. C. 20234

The triboellipsometric apparatus herein described is similar to that used by Laser et. al. (1) The unit is specifically designed to effectively remove, by mechanical polishing, a corrosion or passive film which may have formed on a specimen in a simulated service environment. Ellipsometric and electrochemical measurements on the abraded specimen can be initiated within 1ms of the cessation of polishing after rapid displacement of the polishing arbor away from the specimen surface. Thus, surface film regrowth kinetics may be effectively examined at a much earlier stage than has been heretofore possible. (2)

Mechanical and Electrical systems: Figure 1 shows the disposition of mechanical and electrical components. The components are mounted on a massive frame and are physically separate from the ellipsometer base upon which the PTFE-lined speciman cell is mounted. This arrangement minimizes the transmission of vibration to the specimen. The spindle (g) operates at 300 rpm and is coupled to the drive shaft (m) by means of a spindle connector (e). The spindle connector is supported on the drive shaft by four rows of ball bearings as shown in Section AA. The rows of ball bearings are physically locked to the spindle connector and one of the rows engages a longitudinal slot in the drive shaft. Thus, while being rotated, the drive shaft is free to move longitudinally to compress the spindle pressure spring. A similar "ball bushing" device is utilized to connect the drive pulley (d) to the drive shaft and allows both rotational and longitudinal movement of the drive shaft. The drive pulley is coupled to the electric motor (n) by means of a toothed belt and speed reduction pulley. The polishing arbor is fitted with a sponge rubber pad and nylon lap cloth impregnated with 3μm diamond paste.

The electrical circuitry is shown in Figure 2. The unit features a control for varying the abrasion time between 5 and 15 seconds and an externally available output pulse which can be used to trigger the storage oscilloscope used for recording.

Operational Details: With the polishing spindle in the fully retracted position, the specimen is aligned for maximum reflection of incident light into a photomultiplier tube (PMT). The input light is modulated at 1kHz and the PMT signal synchronously processed with a lock-in-amplifier.

An electric motor (n) is activated and a preselected pulse of from 5-15 sec. is applied to solenoid (a). This causes the driveshaft (m) to

move forward and the polishing arbor (k) to contact the specimen (h). The amount of force applied to the speciman can be varied by altering the compression of the spring within (e). This, in turn, is accomplished by adjusting the position of, and thus the plunger stroke of solenoid (a). When the preset polishing time has elapsed, solenoid (a) is deenergized and a 200 ms pulse applied to solenoid (f). A triggering signal is simultaneously transmitted to the recording oscilloscope. The armature within (f) is accelerated to the rear and ultimately strikes the spindle connector (e). The consequent momentum transfer results in a rapid spindle retract.

The oscilloscope trace shown in Figure 3 indicates the sequence of events when solenoid (f) is energized. The upper left horizontal portion of the trace represents the travel time required before armature (o) strikes connector (e). Since the light path is blocked by the polishing arbor, no PMT signal is observed. As the arbor is retracted the PMT intensity increases and reaches a maximum within ∿0.75ms. Thus, film regrowth studies can be initiated ∿1ms after polishing ceases.

References

1. D. Laser, M. Yaniv and S. Gottesfeld, J. Electrochemical Soc. 125, 358 (1978).

2. J. R. Ambrose and J. Kruger, Corrosion, 28, 30 (1971).

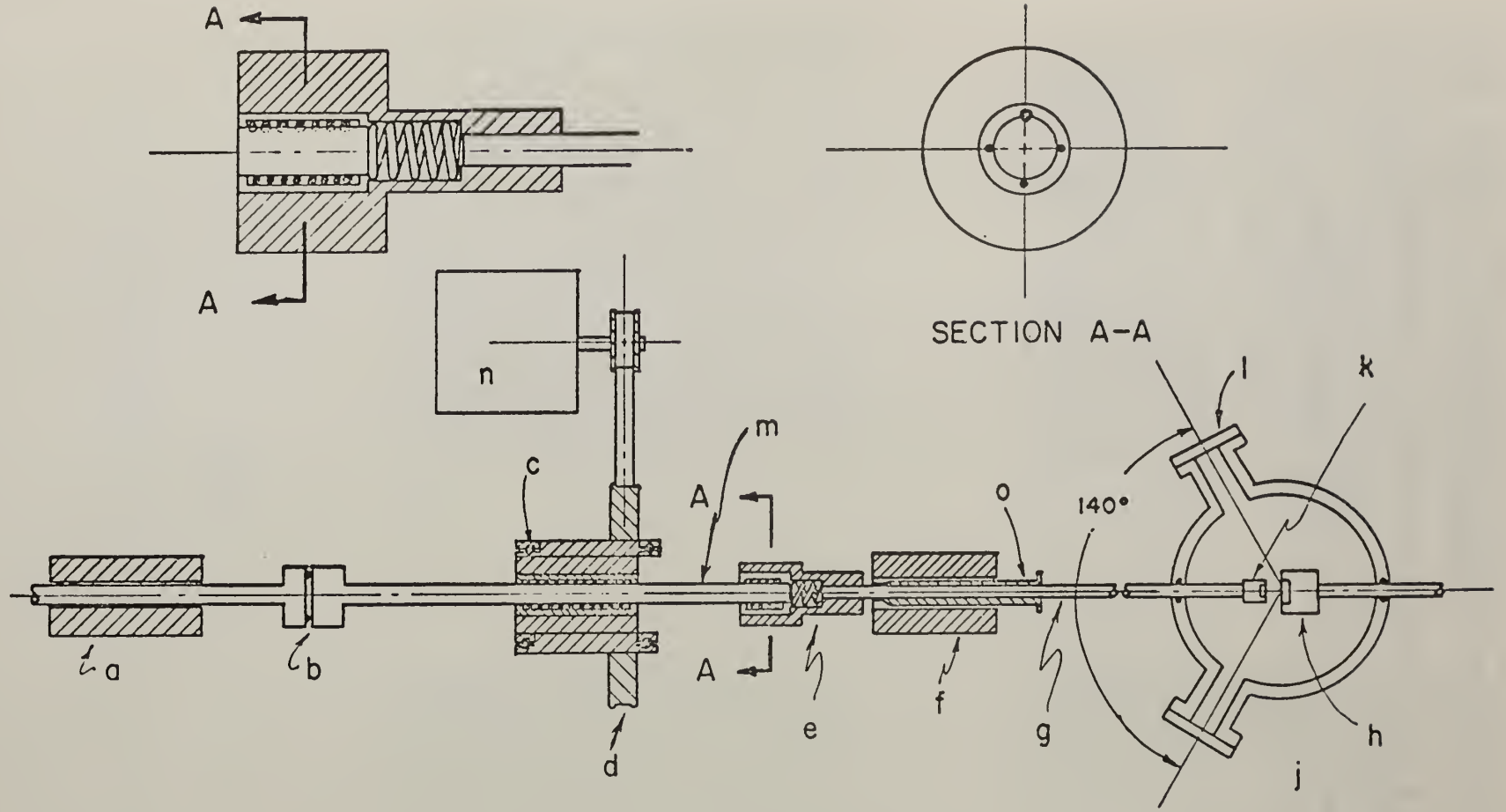

a) PUSH SOLENOID
b) THRUST BEARING
c) DRIVE PULLEY SUPPORT BEARING
d) DRIVE PULLEY
e) SPINDLE CONNECTOR
f) RETRACT SOLENOID
g) SPINDLE
h) SPECIMEN IN EPOXY
j) CELL
k) POLISHING ARBOR
l) OPTICAL PORT
m) DRIVE SHAFT
n) MOTOR
o) ARMATURE

Figure 1. Schematic Arrangement of Mechanical and Electrical Components

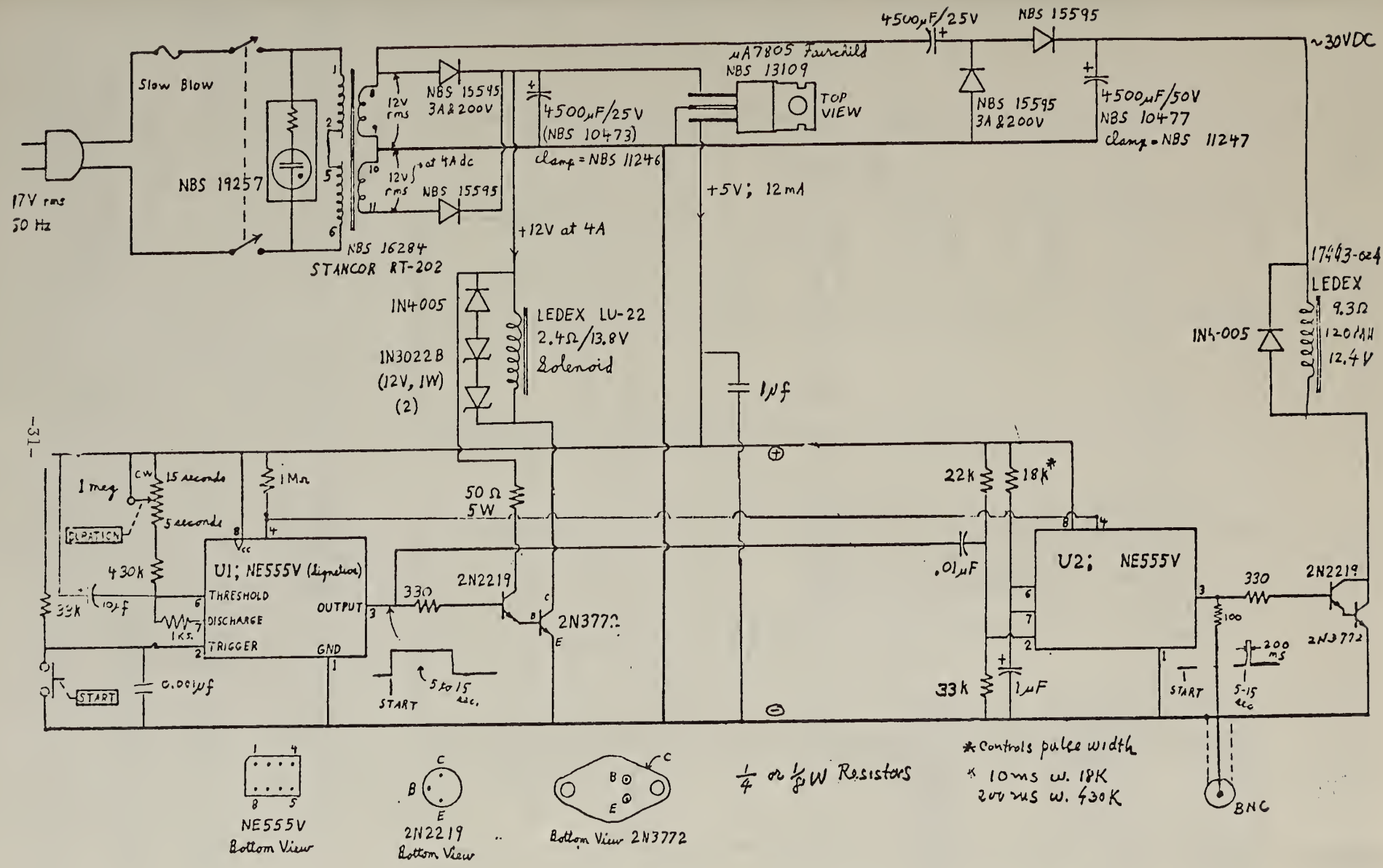

Figure 2. Electrical Schematic

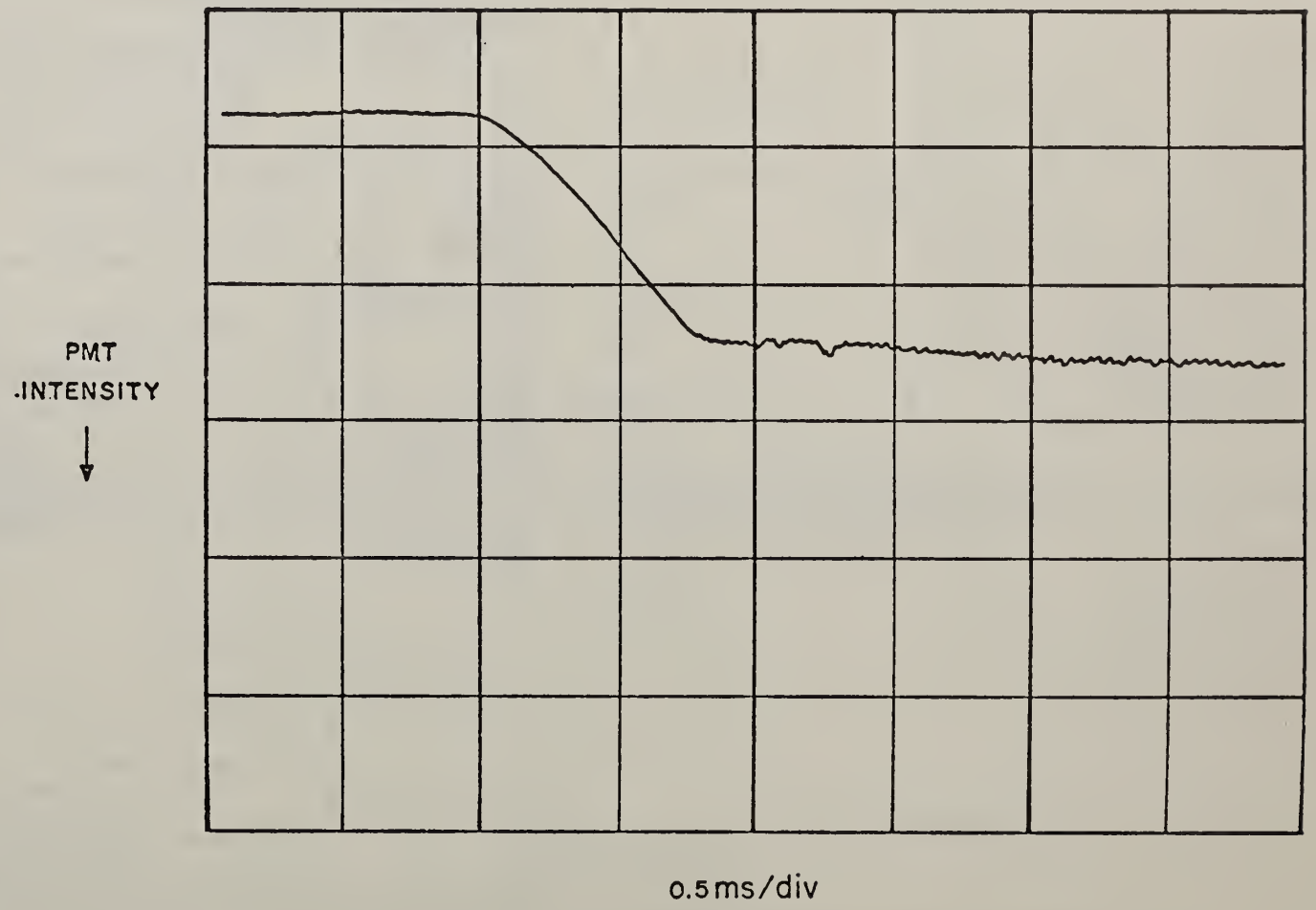

Figure 3. Oscilloscope Trace of PMT Response to Polishing Arbor Retraction

NBS-114A (REV. 9-78)

U.S. DEPT. OF COMM. BIBLIOGRAPHIC DATA SHEET	1. PUBLICATION OR REPORT NO. NBS IR 79-1904	2. Gov't. Accession No.	3. Recipient's Accession No.

4. TITLE AND SUBTITLE

Passive Films, Surface Structure and Stress Corrosion and Crevice Corrosion Susceptibility

5. Publication Date

November 1979

6. Performing Organization Code

7. AUTHOR(S)

J. Kruger, J. J. Carroll, A. J. Melmed, J. J. Ritter, and J. R. Ambrose

8. Performing Organ. Report No.

9. PERFORMING ORGANIZATION NAME AND ADDRESS

NATIONAL BUREAU OF STANDARDS
DEPARTMENT OF COMMERCE
WASHINGTON, DC 20234

10. Project/Task/Work Unit No.

5610448

11. Contract/Grant No.

NAONR 18-69, NR036-082

12. SPONSORING ORGANIZATION NAME AND COMPLETE ADDRESS *(Street, City, State, ZIP)*

Office of Naval Research
Department of the Navy
Arlington, VA 22217

13. Type of Report & Period Covered

interim 12/77-12/78

14. Sponsoring Agency Code

15. SUPPLEMENTARY NOTES

☐ Document describes a computer program; SF-185, FIPS Software Summary, is attached.

16. ABSTRACT *(A 200-word or less factual summary of most significant information. If document includes a significant bibliography or literature survey, mention it here.)*

Field ion microscopy studies of the effects of hydrogen interactions with niobium, aluminum, 304 stainless steel and Fe-24% Cr steel were carried out. Both Nb and Al exposed to hydrogen at 80 K and 30 K respectively showed significant surface disarray, but the effects were not deep or crystallographically selective. The 304 stainless steel show some indications of crystallographically selective attack. Cathodically charged Fe-24% Cr showed a broad spectrum of effects.

A new triboellipsometric apparatus which is capable of measuring repassivation events occurring in times of the order of 0.1 ms is described.

17. KEY WORDS *(six to twelve entries; alphabetical order; capitalize only the first letter of the first key word unless a proper name; separated by semicolons)*

Aluminum; field ion microscopy; iron-chromium alloys; niobium; repassivation kinetics; stainless steel; triboellipsometry

18. AVAILABILITY ☒ Unlimited

☐ For Official Distribution. Do Not Release to NTIS

☐ Order From Sup. of Doc., U.S. Government Printing Office, Washington, DC 20402, SD Stock No. SN003-003-

☒ Order From National Technical Information Service (NTIS), Springfield, VA. 22161

19. SECURITY CLASS (THIS REPORT)	21. NO. OF PRINTED PAGES
UNCLASSIFIED	34
20. SECURITY CLASS (THIS PAGE)	**22. Price**
UNCLASSIFIED	$4.50

USCOMM-DC